Check for updates

Lipid bilayer-mediated spatiotemporal correlation between near-wall confined motion of micro-carriers

Wei Liu,[a] Jinwei Zhong,[a] Pui Wo Felix Yeung, [b] Xiahui Xiao,[a] Yuwei Zhu [*a] and To Ngai [*b]

We employed intensity fluctuations of evanescent light scattering to probe spatiotemporal correlations in the near-wall confined motion of microspheres on supported lipid bilayers (SLBs). Normalized cross-correlation analysis revealed long-range, time-resolved correlations in particle–wall separation distances, demonstrating that interfacial stress propagation can transmit mechanical signals across membrane interfaces. The motion exhibited broadly corralled diffusion, with both the corral size and diffusion constant confined to the nanoscale. This confinement could be further classified into fast and slow modes, with most diffusion constants residing in the slow regime, indicating that SLBs predominantly retard and localize microsphere dynamics at the interface. Furthermore, a transition in the interbilayer interaction profile—from bimodal to single-peak behavior—introduced a characteristic length scale and a kT-scale energy barrier, underscoring the cooperative interplay between interfacial stress propagation and membrane shape remodeling.

Introduction

Cellular membranes are fundamental to a wide range of biological processes.[1–3] For instance, they serve as the outermost barrier, protecting the intracellular cytoplasm and organizing essential components such as genetic material. Within cells, biomembranes enable compartmentalization into subcellular organelles, supporting complex yet highly organized biochemical activities. Notably, membranes also function as two-dimensional (2D) platforms for critical cellular processes such as signal transduction, by facilitating the lateral diffusion and clustering of lipids, proteins, and other macromolecules.[4] This diffusive behavior plays a key role in modulating reaction kinetics and mediating intermolecular interactions, including ligand–receptor recognition.[5–7]

Among membrane properties, the viscosity of lipid bilayers critically governs the length and time scales of diffusion-driven processes.[8,9] For 2D systems/interfaces, the effective viscosity η can be quantitatively related to the diffusion constant D via the Stokes–Einstein relation

$$D = \mu k_B T \propto \eta^{-1} k_B T \qquad (1)$$

[a] *The Key Laboratory of Synthetic and Biological Colloids, Ministry of Education & School of Chemical and Material Engineering, Jiangnan University, Wuxi 214122, P.R. China. E-mail: uvyzhu@gmail.com*

[b] *Department of Chemistry, The Chinese University of Hong Kong, Shatin, N.T., Hong Kong 999077, P.R. China. E-mail: tongai@cuhk.edu.hk*

where μ is a translational or rotational hydrodynamic mobility, k_B (or k) is the Boltzmann constant and T is the temperature. In densely crowded membranes, microscopic inclusions often exhibit slowed or anomalous diffusion, as revealed by lateral mean squared displacement (MSD) measurements.[10,11] This behavior is typically characterized by a nonlinear time dependence

$$\langle \delta^2(\varDelta) \rangle = 4D_\alpha \varDelta^\alpha \quad \text{with} \quad 0 < \alpha < 1 \qquad (2)$$

where α is the anomalous diffusion exponent and D_α is the generalized diffusion constant of physical dimension $m^2\ s^{-\alpha}$. The decoupling of two distinct characteristic timescales in the diffusional motion has been attributed to local heterogeneity within cellular membranes.[10,12] Specifically, the long-time regime reflects the dynamics of the global continuous phase, while the short-time regime captures local fluidity within heterogeneous microdomains such as cholesterol-enriched lipid rafts. Thus, anomalous diffusion across different timescales fundamentally arises from spatial heterogeneity under 2D confinement.

While lateral diffusivity on lipid membranes—including planar and colloidal-supported lipid bilayers (SLBs and CSLBs, respectively)—has been extensively characterized using single-molecule and single-particle tracking techniques,[12–17] far less is known about how micro- and nanoscale carriers diffuse near membrane surfaces and subsequently interact with or fuse into the membranes, particularly in the normal direction when two

lipid bilayers approach one another. A microscopic understanding of SLB approach, adhesion, spreading, and the formation of negative curvature and hemifusion intermediates is essential for elucidating the physical basis of cell–cell communication, endocytosis, and exosome transport, as well as for advancing the development of liposome-based antitumor therapies. Probing membrane interactions requires measurements on well-controlled systems that closely mimic natural conditions, where fluctuations play a critical role. Neutron and X-ray scattering have been employed to investigate the interaction potential between two lipid bilayers, where one adsorbed on a solid surface and the other floating close by.[18,19] Total internal reflection microscopy (TIRM) has also been used to directly quantify the kT-scale interactions between lipid bilayers by monitoring the lateral diffusion and z-directional fluctuations of SLB-modified colloids near membrane surfaces.[20,21] In addition, simulations provide powerful tools for probing biomolecular diffusivity, phase separation, membrane fusion, and vesicle–membrane interactions.[22–26] Collectively, these approaches underscore the central importance of membrane shape remodeling during membrane–membrane interactions.

Importantly, lipid membranes are inherently non-planar, exhibiting three-dimensional (3D) architectures such as cap-like protrusions and bulged domains.[27] These micro- and nanostructures, shaped by intrinsic curvature, offer unique opportunities for membrane-mediated interactions. The presence of such protrusions has been confirmed by 3D single-particle tracking and confocal imaging.[16,20,28] In parallel, lipid membranes are quasi-2D materials with intrinsic heterogeneity and phase separation. Cholesterol-enriched lipid raft domains are randomly embedded across the membrane surface. Previous studies have shown that cholesterol modulates the bending modulus of lipid bilayers, and membrane bending is widely recognized as a critical early step in fusion processes.[29–31] Therefore, elucidating z-directional diffusivity and transient local deformations during bilayer approach is essential for understanding membrane shape remodeling and the principles underlying interbilayer interactions.

In this study, we aim to elucidate—at least in part—the z-directional diffusive behavior and interbilayer interactions that arise when two lipid bilayers approach one another. To this end, we employed a classical ternary lipid system composed of saturated 1,2-dipalmitoyl-sn-glycero-3-phosphocholine (DPPC), unsaturated 1,2-dioleoyl-sn-glycero-3-phosphocholine (DOPC), and cholesterol at a fixed molar ratio of 3:1:1, supported on 3 μm polymeric microspheres and planar glass substrates. Using TIRM, a scattering-based technique,[32–34] we imaged fluctuations in the z-directional displacement of microspheres near the interface, enabling quantitative extraction of diffusion parameters and interbilayer interaction potentials (see Fig. 1). Remarkably, we observed long-range correlations in the confined motion of microspheres separated by distances exceeding 100 μm. Furthermore, we characterized the temporal evolution, or aging, of both the correlated diffusivity and the interbilayer potential energy over the course of the observation period. Our results suggest that interfacial stress, membrane elasticity, and
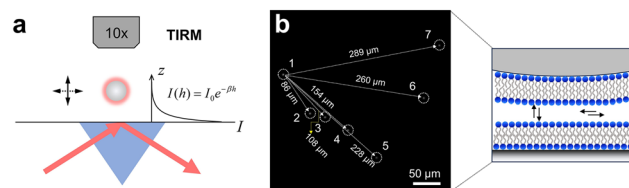

Fig. 1 Schematics for observing the z-directional diffusivity and interbilayer interaction by evanescent wave scattering-based microscopy. (a) Principle of the total internal reflection microscopy (TIRM). (b) Spatial distribution of microspheres (particles 1–7) on the surface of supported lipid bilayer. Right panel: Interbilayer configuration.

dynamic remodeling play critical roles in facilitating the long-range transmission of mechanical signals across cellular membranes.

Experimental

Preparation of liposomes

We employed a ternary lipid mixture—1,2-dipalmitoyl-sn-glycero-3-phosphocholine (DPPC, 99%, Macklin), 1,2-dioleoyl-sn-glycero-3-phosphocholine (DOPC, > 99%, Aladdin), and cholesterol (≥99%, Macklin)—as a model membrane system. Specifically, 0.0100 g DPPC and 0.0035 g DOPC were weighed into a reagent vial. Separately, 0.3867 g powdered cholesterol was dissolved in 1 mL of a mixed organic solvent (cyclohexane/ethanol = 19:1, v/v) to prepare a stock solution at 1 mmol mL^{-1}. A volume of 4.45 μL of this cholesterol stock was added to the lipid mixture, followed by 11.813 mL of the same mixed solvent. The solution was sonicated to facilitate dissolution, yielding a liposome sample with a final concentration of 2×10^{-3} mmol mL^{-1} and a molar ratio of 20%. To remove impurities, the solution was filtered three times using a 0.22 μm Nylon membrane.

Preparation of colloidal supported lipid bilayers

A volume of 12 μL of lipid solution was added to a sample vial and dried under nitrogen to remove the organic solvent, forming a lipid film with a transparent center and white edges. Then, 100 mM NaCl was added, and the sample was sonicated (5 min) to disperse the lipids in water. The mixture was incubated in a 60 °C water bath for 1 h to form liposomes. Subsequently, 1 μL of PS microspheres (3.1 μm diameter, 8% solids, Thermo Fisher Scientific) was added. After 30 min of incubation, the sample was shaken for another 30 min to yield lipid-coated PS particles (i.e., CSLBs). Upon heating above the lipid phase transition temperature, lipid molecules became more fluid and loosely packed, forming a liquid phase with enhanced mobility.

Hydrophilic treatment of glass substrates

Glass slides (25 × 75 × 1 mm, Fisher Scientific) were immersed in piranha solution (H$_2$SO$_4$/H$_2$O$_2$ = 3:1, v/v) and treated for 2 h. Afterward, they were rinsed with deionized water to remove residual piranha solution. The slides were then cleaned three times with deionized water and absolute ethanol, each followed

by 15 min of sonication. Finally, the slides were dried under nitrogen and treated with plasma for 5 min (PDC-002, Harrick Plasma, USA).

Formation of supported lipid bilayers on glass substrates

Supported lipid bilayers were fabricated using the Langmuir–Blodgett (LB) technique.[35] After instrument calibration, the prepared lipid solution was deposited onto the air–water interface. Upon solvent evaporation and stabilization at ~ 1 mN m^{-1} surface pressure for 30 min, the monolayer was compressed at 10 mm min^{-1} until the surface pressure reached 40 mN m^{-1}. The first monolayer was transferred onto the glass substrate *via* vertical lifting at 2 mm min^{-1}. The second monolayer was prepared similarly and deposited by vertical immersion at 2 mm min^{-1} using a PTFE trough, maintaining the bilayer in an aqueous environment.

Principle of total internal reflection microscopy

The central of the technique of TIRM is the application of evanescent wave, which allows it to measure kT-scale interaction between a colloidal microsphere and a flat transparent surface with outstanding distance resolution in direction normal to the wall.[32,34,36–39] In principle, the evanescent wave or field is generated by total reflection of a laser beam at an interface of glass slide and solution. The intensity of scattering light I exponentially decays with a separation distance h from the interface, expressed as[34]

$$I(h) = I_0 e^{-h/d_p} \tag{3}$$

where d_p is the penetration depth, expressed as

$$d_p = \lambda \left/ \left[4\pi \sqrt{(n_1 \sin \theta)^2 - n_2^2} \right] \right. \tag{4}$$

where λ is the laser wavelength, ϑ is the incident angle, n_1 and n_2 are the refractive indexes of prism (material: N-BK7) and sample solutions (*i.e.*, aqueous solutions), respectively.

Therefore, in a typical TIRM measurement, the separation distance between the interface and the particle can be given by eqn (3) as

$$h = -\frac{\ln\left(\dfrac{I(h)}{I_0}\right)}{\beta} \tag{5}$$

where I_0 is the maximum scattering intensity of the particles that have reached the surface. Regarding the collection and processing of the signal, a photomultiplier tube or a high-speed charge coupled device is utilized for capturing the signal from the scattering particles. Then, based on the Boltzmann statistics, the particle–surface interactions can be calculated from the position distribution of a fluctuating particle along the z direction, given by[34,38,39]

$$p(h) = A e^{\frac{-\phi(h)}{kT}} \tag{6}$$

where A is a normalization constant related to the total number of height observations, ϕ is the interaction potential, $p(h)$ is the probability of finding a particle at a certain height, k is the Boltzmann constant, and T is the temperature. Instead of measuring an absolute value of the interaction potential, the potential measured with TIRM is usually a comparative value, given by

$$\frac{\phi(h) - \phi(h_{\text{ref}})}{kT} = \ln \frac{p(h_{\text{ref}})}{p(h)} \tag{7}$$

where h_{ref} is often chosen as h_m, which represents the separation distance with the lowest potential energy. By measuring the number of times a particle samples each height during the course of an experiment, a particle height histogram, $n(h)$, can be measured from the time dependent height fluctuations, *i.e.*, $h(t) \rightarrow n(h)$. With a large enough number of observations to ensure sufficient statistical sampling, $n(h)$ can be considered a good approximation of the probability density of heights, $p(h)$. The interaction potential at the separation distance where the particle appears most frequently is recognized as the 'zero' point of the interaction curve, can be given by[34,38,39]

$$\frac{\phi(h) - \phi(h_m)}{kT} = \ln \frac{n(h_m)}{n(h)} \tag{8}$$

TIRM-based measurement of inter-bilayer interactions

To measure inter-bilayer interactions using TIRM, a flow cell was assembled with a 20% cholesterol-containing lipid-coated slide. The air-exposed surface was cleaned with mixed solvent, rinsed with ethanol and water, and dried under nitrogen. Immersion oil was applied to the cleaned surface, and the slide was tightly coupled to a 70° prism to avoid air bubbles. The flow cell was placed on the microscope stage and connected to a syringe pump. A 20 mL volume of 100 mM NaCl was injected to replace ultrapure water in the cell. Cholesterol content on both the slide and PS particles was varied to modulate system conditions.

Lipid-coated PS particles (CSLBs) were loaded into a syringe and introduced into the inverted flow cell. The sample was washed with 20 mL of 100 mM NaCl at 1 mL min^{-1}. After washing, the flow cell was returned to its upright position to begin imaging. Images were recorded in dynamic range mode with gain set to 16-bit, ROI at 512 × 512 pixels and exposure time of 10 ms (Kinetix22, Teledyne Photometrics Inc., US). Seven spatially distinct particles were tracked, with a total of 30 000 frames captured. Imaging was repeated every 20 min, with the final time point at 80 min. The images were processed based on the radial symmetry method under particle-tracking framework using previously reported MATLAB program.[40]

Results and discussion

Spatiotemporal correlation of confined motion

We first examined the spatiotemporal correlations in the scattered intensity and height profiles of microspheres (particles 1–7, P1–7 in Fig. 2). A total of N = 30 000 images (512 × 512 pixels) were acquired at a sampling rate of 100 frames

per second, corresponding to an exposure time of 10 ms. To mimic physiological conditions and screen electrostatic repulsion between lipid bilayers (zeta potential ~ -50 mV), an aqueous solution containing 100 mM NaCl was used—potentially facilitating membrane fusion or remodeling.

Fig. 2a present representative z-directional trajectories over time (see Fig. S1 for more trajectories). Upon injection, microspheres rapidly settled onto the surface of the SLBs, where interbilayer separations h_0 ranged from ~ 10 to 50 nm. Short-timescale stochastic fluctuations (~ 200–400 ms) were confined within a narrow range of ~ 2–3 nm (background noise ≤ 1 nm, data not shown), consistent with lipid bilayer-mediated confinement. This strictly limited motion echoes findings from our previous study involving SLBs under basic pH conditions.[41] Interestingly, beyond these small-scale fluctuations, we observed transient displacements from the equilibrium position. These events manifested as sudden, step-like "jumps" of several nanometers, with dwell times ranging from 10 to 15 seconds or longer. Such behavior may arise from non-specific interactions, potentially driven by microdomain-induced affinity between the two bilayers.[42,43]

Notably, we observed a striking correlation in the z-directional displacements—particularly the step-like "jumps"—among the seven microspheres of interest. These correlated motions were not attributable to background vibrations, which were carefully ruled out: no such correlation was detected on bare microsphere surfaces or substrates lacking lipid membranes (Fig. S2). As previously discussed, cholesterol increases the bending modulus of cellular membranes and may also enhance the elasticity and interfacial tension of the SLBs. This increased elasticity likely facilitates interfacial stress propagation, enabling pulse-like mechanical signals to be transmitted across the membrane interface.[44–47]

To quantitatively assess the degree of correlation between the z-directional displacements of CSLBs, we employed a normalized cross-correlation function (CCF) applied to pairs of time-resolved intensity signals (e.g., I_i and I_j)[48,49]

$$\text{CCF}^{(i,j)} = G^{(i,j)}(\tau) = \frac{\langle \delta I_i(t+\tau) \cdot \delta I_j(t) \rangle_t}{\langle I_i(t) \rangle_t \cdot \langle I_j(t) \rangle_t} \tag{9}$$

where $\langle \cdot \rangle$ denotes the time average, τ is the lag time between the two time series signals, and $\delta I = I - \langle I \rangle$. Fig. 2b shows the cross-correlations profiles on lipid bilayers, using the intensity signal of particle 1 (I_1) as the reference. $G^{(i,j)}(\tau)$ decayed rapidly with a characteristic correlation time τ_D ranging from few to tens of
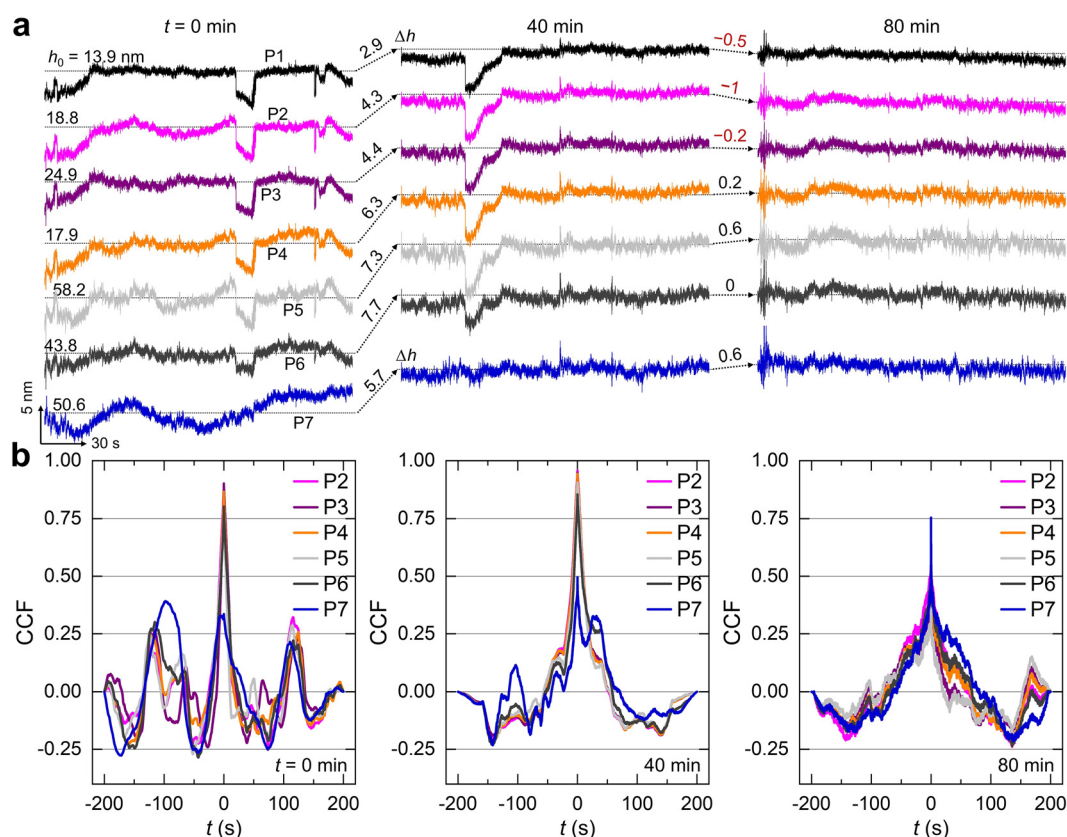

Fig. 2 Spatiotemporal correlation in the near-wall diffusions. (a) Representative trajectory of the z-directional displacements of particles 1–7 (P1–7) at different points in time. Horizonal dotted lines represent the equilibrium height h_0 for each particle. Δh denotes the changes in h_0, indicated by the numbers (in unit of nm) above the dotted arrows. (b) Normalized cross-correlation functions (CCF) using signals of P1 as the reference. $t < 0$ represents the negative lag time.
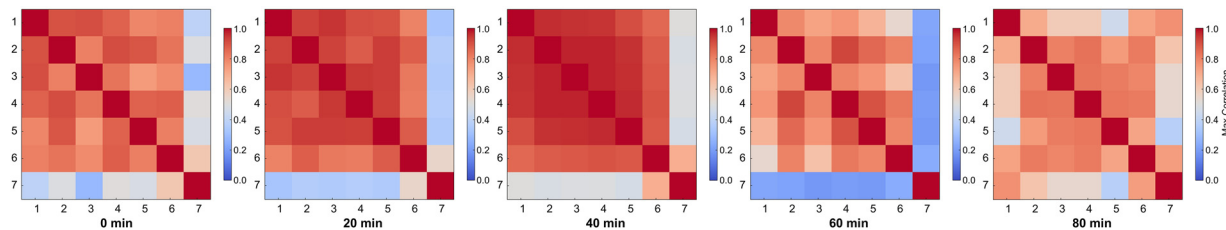
Fig. 3 Two-dimensional distribution of the cross-correlations at zero lag time $G(0)$. Numbers along the x and y coordinates represent the seven microspheres of interest (P1–7). Color bar indicates the value of $G(0)$.

seconds (see Fig. S3 for more CCF). At zero lag, *i.e.*, $\tau = 0$, a higher cross-correlation value $G(0)$ was observed among particles P1 to P6, suggesting that shorter spatial separation between microspheres (Fig. 1b) enhances intensity-fluctuation similarity.

To further visualize this effect, we plotted the 2D distribution of $G(0)$ for all microspheres across different observation times (Fig. 3). Notably, $G(0)$ values among particles P1 to P6 were much larger than $G^{(i=1–6,j=7)}(0)$, where the former increased over time, peaked around 40 minutes, and gradually declined thereafter. Specifically, for P7, we observed relatively stronger correlation after a longer period, with $G(0) > 0.75$ at 80 min (Fig. S3, right-bottom panel). This temporal evolution of cross-correlation suggests that z-directional displacement and diffusivity between the two approaching bilayers are both long-range (>100 μm) and time-resolved, dynamically evolving over tens of minutes. Such behavior may arise from lipid exchange or the transient formation of bridging structures between bilayers. These events could propagate rapidly across the membrane surface *via* interfacial tension, potentially giving rise to the observed spatiotemporal correlations.[44,50] The relatively weaker and unstable correlation observed for P7 likely reflects the finite range of propagation and concomitant energy dissipation, compounded by a non-uniform local environment.

Anomalous diffusion

We next evaluate the z-directional diffusive behavior between the two approaching lipid bilayers. To quantify the diffusivity, we calculated the time-averaged MSD for individual particle trajectories at various time intervals[13]

$$\overline{\langle \delta_\tau z_i^2 \rangle} = \frac{1}{t - \tau} \int_0^{t-\tau} \left[z_i(t' + \tau) - z_i(t') \right]^2 dt' \quad (10)$$

where $z_i(t)$ denotes the separation distance between particle i and the substrate at time t and $\tau \ll t$. Instead of the subdiffusive behavior described by eqn (2), a broadly corralled diffusion pattern was observed. The MSD curves exhibit confinement within a corralled boundary (Fig. 4a) and, in some cases, display an abrupt change in slope after a characteristic timescale (see MSD curves at $t = 0$ s, 170 s, 1200 s, 2438 s, and 4910 s in Fig. S4). To quantitatively extract the diffusion coefficient within the corralled region, we employed an exponentially
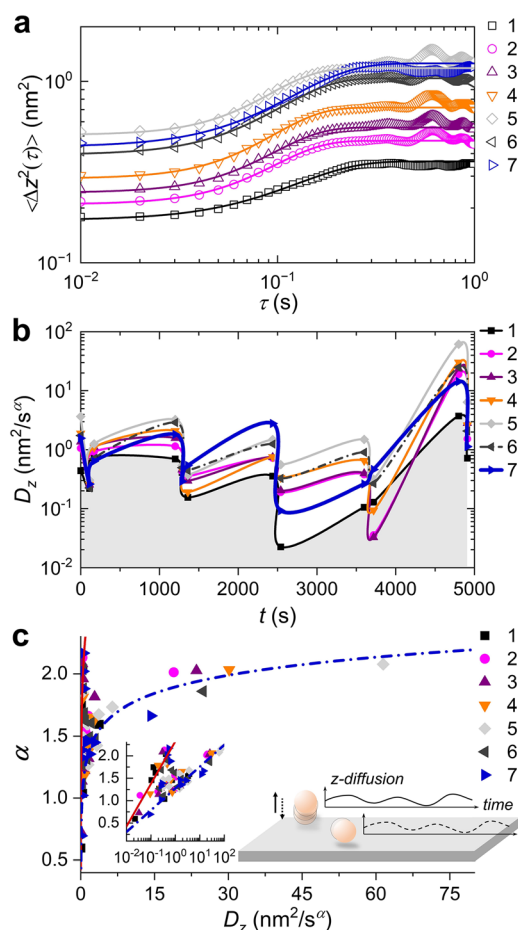

Fig. 4 Anomalous diffusion in the z-direction. (a) Representative mean squared displacements of the seven microspheres of interest. Solid lines represent the non-linear fitting by eqn (11) for corralled diffusion with a relaxed power-law exponent. (b) Time-evolution of the diffusion constants D_z. Lines are drawn for guides of eye. (c) Diffusivity in the fast (dashed dotted line) and slow mode (solid line). Inset: Semi-log plot of D_z versus α. Right-bottom: Stochastic collision between two approaching lipid bilayers.

decaying analytical form of the MSD curves with a relaxed power-law index[51]

$$\langle \Delta z^2 \rangle = \langle z_c^2 \rangle \left[1 - A_1 \exp\left(\frac{-2D_z \tau^\alpha}{\langle z_c^2 \rangle} \right) \right] \quad (11)$$

Paper

Soft Matter

where $\langle z_c^2 \rangle$ denotes the corral size, A_1 is a parameter determined by the corral geometry, and D_z is the diffusion constant in the normal direction. Fig. 4b shows the time-resolved D_z for each particle (see Fig. S5 for z_c and α). The diffusion exhibited pronounced fluctuations throughout the observation period. Similar to the z-directional displacements, the temporal variation of D_z was nearly correlated across all microspheres (lower correlation for P7), reflecting synchronized confined motion mediated by the soft interfaces constituted of two lipid bilayers.

It is noteworthy that the D_z values are nearly six to seven orders of magnitude lower than those of lipids or proteins diffusing within membranes.[12,13,17] Considering the inverse relationship between diffusion coefficient D and particle size a (Stokes–Einstein relation, $D \sim k_B T/a$), the diffusivity of a microscale particle is expected to be approximately three orders of magnitude lower than that of nanoscale biomolecules. In addition, for near-wall confined diffusion, Bevan and Prieve[38] provided a drag correction factor, $\beta_\perp$, as a close approximation to Brenner's infinite series solution,[52] reported that

$$\beta_\perp \equiv D_\perp/D_0 \approx \frac{6(h/a)^2 + 2h/a}{6(h/a)^2 + 9h/a + 2} \quad (12)$$

where h is the particle–wall separation distance, approximately represented by the equilibrium height h_0. For $h_0/a \sim 0.01$, we obtained $\beta_\perp \sim 10^{-2}$, indicating that the diffusion coefficient is reduced by an additional two orders of magnitude due to near-wall hindrance.[32,53] The remaining suppression (a further reduction of one to two orders of magnitude in D) can be attributed to the SLBs, suggesting that interbilayer interactions substantially inhibit the confined motion of CSLBs, likely through lipid bilayer adhesion, fusion, and spreading.[20]

Furthermore, the diffusive behavior of confined motion can be classified into two distinct regimes—a fast mode and a slow mode—based on the relationship of D_z-versus-α (Fig. 4c). The corralled diffusion follows a power-law dependence, expressed as

$$\alpha \sim 2.302\varsigma \ln D_z \quad (13)$$

where ς is the scaling exponent. We determined $\varsigma \sim 0.412$ for the slow mode and $\varsigma \sim 0.211$ for the fast mode. The majority of D_z fell within the slow mode regime, indicating that the two lipid bilayers predominantly confine, retard, and localize microsphere diffusion at the interface. In contrast, the fast mode may reflect conformational changes in membrane shape at the contact region, where the bilayers stochastically and repeatedly collide. The emergence of bending or bulging structures likely relaxes confinement, creating a more flexible interfacial space and enabling faster diffusion.[54–56] Notably, similar fast and slow anomalous diffusion behaviors have been reported in cellular membranes via single-lipid, single-protein,
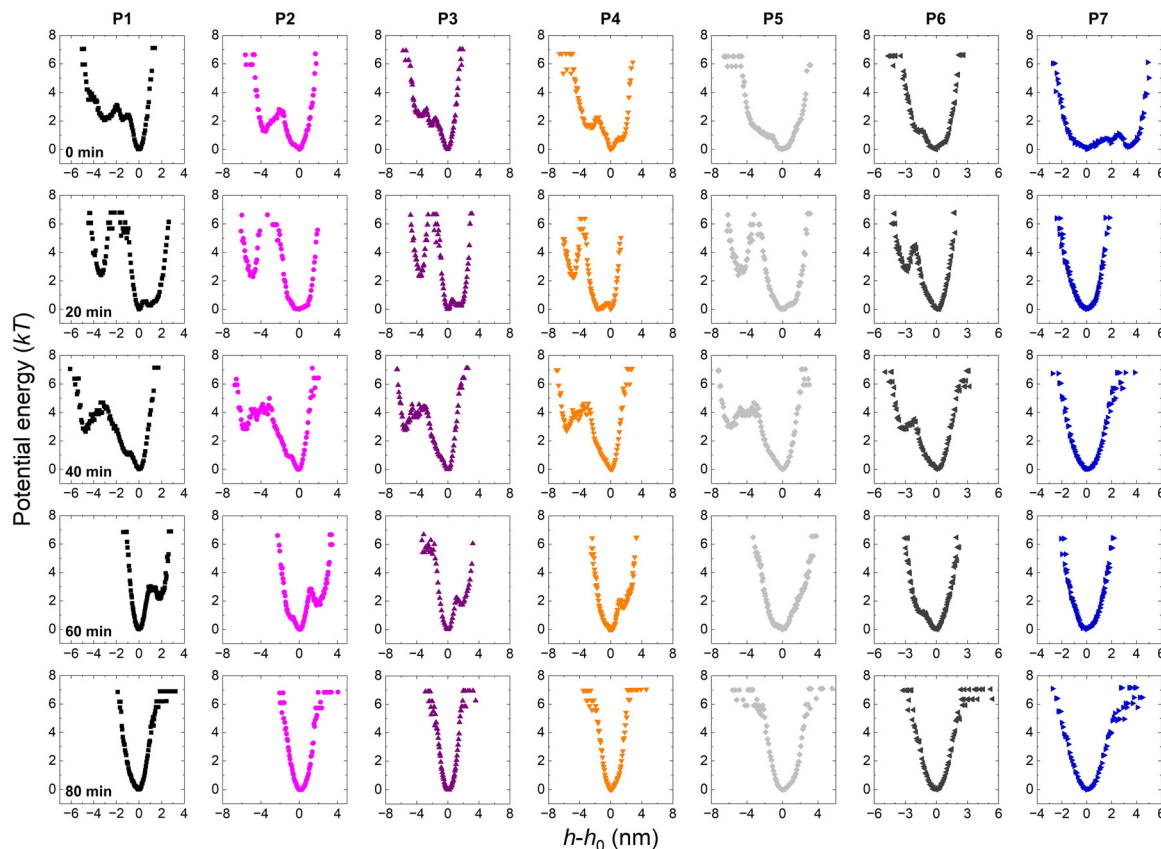

Fig. 5 Potential energy $U(h - h_0)$ for the interacting two lipid bilayers at various observation times. The potentials transitioned from bimodal to single-peak profile. Energy barrier $\Delta\Phi$ was determined by the difference between the two minima in the bimodal distributions.
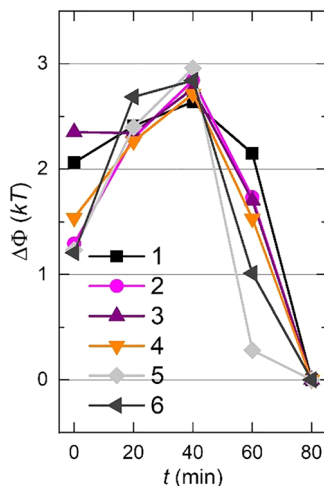
Fig. 6 Plot of the energy barrier $\Delta\Phi$-*versus*-evolution time for particles 1–6.

and single-particle tracking.[10,12,13,16,17] These phenomena are often attributed to phase-separation-induced spatial confinement in crowded quasi-2D fluids. Our findings further suggest that the fast and slow z-directional diffusion modes are closely linked to dynamic membrane shape remodeling.

Potential energy

To further quantify membrane shape remodeling, we analysed the interaction potential energy between the two bilayers—namely, the immobilized planar SLBs on solid substrates and the diffusing CSLBs with intrinsic curvature. Fig. 5 shows the time evolution of the potential energy profiles $U(h - h_0)$ for individual CSLBs, where h_0 denotes the equilibrium height corresponding to the minimum potential. Typically, the profiles transitioned from a bimodal distribution to a single-peak form, suggesting the existence of at least two equilibrium or pseudo-steady states during bilayer approach and deformation. A similar phenomenon was previously reported by Everett and Bevan,[20] who employed TIRM to monitor the spreading of supported lipid bilayers from a wall onto bare 1.5 μm silica particles.

The bimodal-to-single peak transition also revealed a characteristic length scale, defined as the height difference between the two equilibrium positions. Over time, this length scale decreased from approximately 4–6 nm (0–40 min) to ∼2 nm (∼60 min), suggesting a dynamic process evolving from the transient emergence of SLB bulges to eventual bilayer fusion. Notably, this length scale is much narrower than the ∼18 nm separation between potential energy minima as previously reported.[20] Such differences in length scales highlight distinct SLB configurations associated with interbilayer fusion *versus* single bilayer spreading. When considered together with the ∼1 nm corral size (Fig. S5b and c), our findings provide new insight into the fusion mechanism of apposing SLBs at even smaller nanoscales, thereby deepening the microscopic understanding of lipid vesicle–membrane interactions.

Additionally, a kT-scale energy barrier $\Delta\Phi$ between transitional membrane fusion configurations—defined as the energy difference between the two potential energy minima—was quantified (Fig. 6). The value of $\Delta\Phi$ initially increased, reaching a maximum of approximately $3kT$ around 40 min, before gradually declining to zero. This temporal evolution suggests that transient structural rearrangements initially stabilize intermediate fusion states, but are eventually relaxed as the bilayers proceed toward complete fusion. Notably, a similar time-dependent trend was observed in the zero-lag cross-correlations $G(0)$, underscoring the coupling between diffusivity correlations and energetic barriers. The coincidence of these behaviors highlights the cooperative interplay between interfacial stress propagation and membrane shape remodeling, indicating that mechanical stresses and elastic deformations act in concert to regulate the kinetics and energetics of bilayer fusion.

Conclusions and discussion

Using total internal reflection microscopy, we uncovered a long-overlooked spatiotemporal correlation in the near-wall confined motion of micro-carriers, where both the particle and wall surfaces were modified with lipid bilayers containing cholesterol (20 mol% in this study). Instead of the typical sublinear diffusion behavior, a corralled diffusion pattern was observed and quantitatively analyzed, offering new insights into diffusive mechanisms in bio-membrane systems. Further analysis of the interbilayer interactions revealed a transition in the potential energy profile from a double-well to a single harmonic-like well, reflecting the time-dependent evolution of fusion configurations.

Overall, this study advances our understanding of membrane shape remodeling. We demonstrate that non-specific interactions can induce transient deformations, such as bulges or cap-like structures,[43,57] thereby providing new experimental evidence for the dynamic mechanisms underlying membrane fusion.[20,21] The observed remodeling of membrane morphology and transitions between multiple equilibrium states highlight the critical roles of elasticity and interfacial tension in regulating local deformations, offering insight into how membranes mechanically respond to external forces or interactions.[58,59] In addition, the discovery of long-range correlated motion of colloidal-supported lipid bilayers suggests that interfacial fluctuations can transmit mechanical signals across large spatial scales, thereby deepening our understanding of mechanical coupling and signal propagation in cellular membranes.[44,50,60] Finally, the identification of fast and slow anomalous diffusivities associated with structural heterogeneity indicates that local membrane inhomogeneity, such as lipid raft domains, may play an essential role in governing membrane–membrane interactions.[26,61]

Beyond membrane remodeling, a quantitative understanding of interbilayer interactions provides valuable guidance for the development of biomimetic membranes, enabling designs
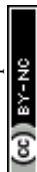
that more closely replicate the stability and functionality of natural cell membranes.[62,63] Insights into adhesion and deformation mechanisms can inform the optimization of liposomal drug-delivery carriers, improving their fusion efficiency with cellular membranes and enhancing targeting and release control. Measurements of interaction potentials and diffusion behaviors also contribute to a more comprehensive explanation of cell–cell contact, adhesion, and signal transmission, supporting progresses in cell biology and immunology.[64–66] Moreover, the observed particle motion patterns offer a model for lipid vesicle–membrane interactions, helping to predict the behavior of liposomes *in vivo* and their binding and penetration into cellular membranes.[67–69]

In summary, our observations collectively suggest that when two lipid bilayers with high internal fluidity approach one another, non-specific interactions can induce the transient formation of bulged structures, most likely protruding from the planar supported lipid bilayers. These dynamic shape changes lead to shifts between distinct equilibrium states in the interbilayer interaction potential. Structural heterogeneity further contributes to the emergence of fast and slow anomalous diffusion behaviors in lipid-bilayer-enveloped microcarriers. Moreover, membrane elasticity and interfacial tension appear to facilitate spatiotemporal correlations in confined motion. Future investigations employing fast, super-resolution imaging techniques to track the *in situ* correlated diffusion of interacting cellular membranes are expected to yield direct evidence of membrane shape remodeling.

Author contributions

Wei Liu: conceptualization, methodology, formal analysis, visualization, supervision, project administration, funding acquisition, writing – original draft. Jinwei Zhong: software, validation, formal analysis, investigation, data curation. Pui Wo Felix Yeung: software, validation, formal analysis. Xiahui Xiao: validation, investigation. Yuwei Zhu: funding acquisition, writing – review & editing. To Ngai: conceptualization, project administration, writing – review & editing.

Conflicts of interest

There are no conflicts to declare.

Data availability

The data supporting this article have been included as part of the supplementary information (SI). Supplementary information is available. See DOI: https://doi.org/10.1039/d5sm01211b.

Acknowledgements

Notes and references

1 S. A. Shelby, I. Castello-Serrano, K. C. Wisser, I. Levental and S. L. Veatch, *Nat. Chem. Biol.*, 2023, **19**, 750–758.
2 X. Cheng and J. C. Smith, *Chem. Rev.*, 2019, **119**, 5849–5880.
3 D. Krapf, *Curr. Opin. Cell Biol.*, 2018, **53**, 15–21.
4 S. J. Singer and G. L. Nicolson, *Science*, 1972, **175**, 720–731.
5 M. Schmick and P. I. Bastiaens, *Cell*, 2014, **156**, 1132–1138.
6 Y. K. Lee, H. Lee and J.-M. Nam, *NPG Asia Mater.*, 2013, **5**, e48.
7 N.-K. Lee, A. Johner, F. Thalmann, L. Cohen-Tannoudji, E. Bertrand, J. Baudry, J. Bibette and C. M. Marques, *Langmuir*, 2008, **24**, 1296–1307.
8 T. T. Hormel, M. A. Reyer and R. Parthasarathy, *Biophys. J.*, 2015, **109**, 732–736.
9 S. Pronk, E. Lindahl and P. M. Kasson, *Nat. Commun.*, 2014, **5**, 3034.
10 Y. Liu, X. Zheng, D. Guan, X. Jiang and G. Hu, *ACS Nano*, 2022, **16**, 16054–16066.
11 J.-H. Jeon, H. M.-S. Monne, M. Javanainen and R. Metzler, *Phys. Rev. Lett.*, 2012, **109**, 188103.
12 X. Xu, C. Xu, W. Zhang, Z. Liu, Y. Wei, K. Yang and B. Yuan, *J. Phys. Chem. B*, 2025, **129**, 5464–5476.
13 L. Gascoigne, R. P. Tas, P. G. Moerman and I. K. Voets, *Soft Matter*, 2025, **21**, 3058–3066.
14 P. Liu and P. J. Beltramo, *Soft Matter*, 2023, **19**, 7708–7716.
15 Y.-J. Chai, C.-Y. Cheng, Y.-H. Liao, C.-H. Lin and C.-L. Hsieh, *Biophys. J.*, 2022, **121**, 3146–3161.
16 Y. Zhong and G. Wang, *Langmuir*, 2018, **34**, 11857–11865.
17 J.-H. Jeon, M. Javanainen, H. Martinez-Seara, R. Metzler and I. Vattulainen, *Phys. Rev. X*, 2016, **6**, 021006.
18 T. Mukhina, A. Hemmerle, V. Rondelli, Y. Gerelli, G. Fragneto, J. Daillant and T. Charitat, *J. Phys. Chem. Lett.*, 2019, **10**, 7195–7199.
19 A. Hemmerle, L. Malaquin, T. Charitat, S. Lecuyer, G. Fragneto and J. Daillant, *Proc. Natl. Acad. Sci. U. S. A.*, 2012, **109**, 19938–19942.
20 W. N. Everett and M. A. Bevan, *Soft Matter*, 2014, **10**, 332–342.
21 W. N. Everett, D. J. Beltran-Villegas and M. A. Bevan, *Langmuir*, 2010, **26**, 18976–18984.
22 S. Pronk, E. Lindahl and P. M. Kasson, *J. Am. Chem. Soc.*, 2015, **137**, 708–714.
23 Y. Zhuo, Z. Luo, Z. Zhu, J. Wang, X. Li, Z. Zhang, C. Guo, B. Wang, D. Nie and Y. Gan, *Nat. Nanotechnol.*, 2024, **19**, 1858–1868.
24 E. Yamamoto, T. Akimoto, A. C. Kalli, K. Yasuoka and M. S. Sansom, *Sci. Adv.*, 2017, **3**, e1601871.
25 M. D. Elola and J. Rodriguez, *J. Phys. Chem. B*, 2018, **122**, 5897–5907.
26 C.-P. Chng, K. J. Hsia and C. Huang, *Soft Matter*, 2022, **18**, 7752–7761.
27 S. Semrau and T. Schmidt, *Soft Matter*, 2009, **5**, 3174–3186.

28 J. C. Stachowiak, C. C. Hayden and D. Y. Sasaki, *Proc. Natl. Acad. Sci. U. S. A.*, 2010, **107**, 7781–7786.

29 F. T. Doole, T. Kumarage, R. Ashkar and M. F. Brown, *J. Membr. Biol.*, 2022, **255**, 385–405.

30 J. F. Nagle, *Phys. Rev. E*, 2021, **104**, 044405.

31 S. Chakraborty, M. Doktorova, T. R. Molugu, F. A. Heberle, H. L. Scott, B. Dzikovski, M. Nagao, L.-R. Stingaciu, R. F. Standaert and F. N. Barrera, *Proc. Natl. Acad. Sci. U. S. A.*, 2020, **117**, 21896–21905.

32 J. Wu, W. Liu and T. Ngai, *Soft Matter*, 2023, **19**, 4611–4627.

33 M. A. Bevan and S. L. Eichmann, *Curr. Opin. Colloid Interface Sci.*, 2011, **16**, 149–157.

34 D. C. Prieve and N. A. Frej, *Langmuir*, 1990, **6**, 396–403.

35 J. Yuan, C. Hao, M. Chen, P. Berini and S. Zou, *Langmuir*, 2013, **29**, 221–227.

36 X. Gong, Z. Wang and T. Ngai, *Chem. Commun.*, 2014, **50**, 6556–6570.

37 L. Liu, A. Woolf, A. W. Rodriguez and F. Capasso, *Proc. Natl. Acad. Sci. U. S. A.*, 2014, **111**, E5609–E5615.

38 M. A. Bevan and D. C. Prieve, *J. Chem. Phys.*, 2000, **113**, 1228–1236.

39 H.-J. Wu and M. A. Bevan, *Langmuir*, 2005, **21**, 1244–1254.

40 F. Cao, J. Wu, Y. Li and T. Ngai, *Langmuir*, 2019, **35**, 8910–8920.

41 W. Liu, Z. Zhao, J. Zhong, P. W. F. Yeung, J. Wu, Y. Li, H. Jiang, Y. Zhu and T. Ngai, *Chem. Sci.*, 2025, **16**, 16625–16637.

42 A. Sardar, N. Dewangan, B. Panda, D. Bhowmick and P. K. Tarafdar, *J. Membr. Biol.*, 2022, **255**, 691–703.

43 H. R. Marsden, I. Tomatsu and A. Kros, *Chem. Soc. Rev.*, 2011, **40**, 1572–1585.

44 R. Dharan, A. Barnoy, A. K. Tsaturyan, A. Grossman, S. Goren, I. Yosibash, D. Nachmias, N. Elia, R. Sorkin and M. M. Kozlov, *Nat. Commun.*, 2025, **16**, 91.

45 C. Aponte-Santamaría, J. Brunken and F. Gräter, *J. Am. Chem. Soc.*, 2017, **139**, 13588–13591.

46 L. U. Brinkmann and J. S. Hub, *Proc. Natl. Acad. Sci. U. S. A.*, 2016, **113**, 10565–10570.

47 A. Botan, L. Joly, N. Fillot and C. Loison, *Langmuir*, 2015, **31**, 12197–12202.

48 C. V. Kelly, D. L. Wakefield, D. A. Holowka, H. G. Craighead and B. A. Baird, *ACS Nano*, 2014, **8**, 7392–7404.

49 S. Wennmalm and J. Widengren, *Anal. Chem.*, 2010, **82**, 5646–5651.

50 Z. Shi, S. Innes-Gold and A. E. Cohen, *Sci. Adv.*, 2022, **8**, eabo1297.

51 M. J. Saxton and K. Jacobson, *Annu. Rev. Biophys. Biomol. Struct.*, 1997, **26**, 373–399.

52 H. Brenner, *Chem. Eng. Sci.*, 1961, **16**, 242–251.

53 J. Wu, F. Cao, P. W. F. Yeung, M. Li, K. Ohno and T. Ngai, *ACS Macro Lett.*, 2024, **13**, 1376–1382.

54 M. M. Kozlov and J. W. Taraska, *Nat. Rev. Mol. Cell Biol.*, 2023, **24**, 63–78.

55 K. Sengupta and A. S. Smith, in *Physics of Biological Membranes*, ed. P. Bassereau and P. Sens, Springer, Cham., 2018.

56 R. Lipowsky, *Nature*, 1991, **349**, 475–481.

57 E. Loiseau, J. A. Schneider, F. C. Keber, C. Pelzl, G. Massiera, G. Salbreux and A. R. Bausch, *Sci. Adv.*, 2016, **2**, e1500465.

58 K. V. Pinigin, *Phys. Rev. E*, 2025, **112**, 055405.

59 Z. Chen, P. Chen, J. Li, E. Landao-Bassonga, J. Papadimitriou, J. Gao, D. Liu, A. Tai, J. Ma and D. Lloyd, *Sci. Adv.*, 2025, **11**, eads6132.

60 H. De Belly, S. Yan, H. B. da Rocha, S. Ichbiah, J. P. Town, P. J. Zager, D. C. Estrada, K. Meyer, H. Turlier, C. Bustamante and O. D. Weiner, *Cell*, 2023, **186**, 3049–3061.

61 G. P. Pattnaik and H. Chakraborty, *Vitamins and hormones*, Elsevier, 2021.

62 T. Rasheed, F. Nabeel, A. Raza, M. Bilal and H. Iqbal, *Mater. Today Chem.*, 2019, **13**, 147–157.

63 M. Sheikhpour, L. Barani and A. Kasaeian, *J. Controlled Release*, 2017, **253**, 97–109.

64 K. Hennig, I. Wang, P. Moreau, L. Valon, S. DeBeco, M. Coppey, Y. Miroshnikova, C. Albiges-Rizo, C. Favard and R. Voituriez, *Sci. Adv.*, 2020, **6**, eaau5670.

65 E. E. Hui and S. N. Bhatia, *Proc. Natl. Acad. Sci. U. S. A.*, 2007, **104**, 5722–5726.

66 C. S. Chen, J. Tan and J. Tien, *Annu. Rev. Biomed. Eng.*, 2004, **6**, 275–302.

67 C. Peetla, A. Stine and V. Labhasetwar, *Mol. Pharm.*, 2009, **6**, 1264–1276.

68 S. Paramshetti, M. Angolkar, S. Talath, R. A. M. Osmani, A. Spandana, A. Al Fatease, U. Hani, K. Ramesh and E. Singh, *Life Sci.*, 2024, **346**, 122616.

69 Y. Chen, N. Douanne, T. Wu, I. Kaur, T. Tsering, A. Erzingatzian, A. Nadeau, D. Juncker, V. Nerguizian and J. V. Burnier, *Sci. Adv.*, 2025, **11**, eads5249.